RESEARCH ARTICLE

GRAVITATIONAL LENSING

Relativistic deflection of background starlight measures the mass of a nearby white dwarf star

Kailash C. Sahu,[1]* Jay Anderson,[1] Stefano Casertano,[1] Howard E. Bond,[2] Pierre Bergeron,[3] Edmund P. Nelan,[1] Laurent Pueyo,[1] Thomas M. Brown,[1] Andrea Bellini,[1] Zoltan G. Levay,[1] Joshua Sokol,[1] Martin Dominik,[4] Annalisa Calamida,[1] Noé Kains,[1] Mario Livio[5]

Gravitational deflection of starlight around the Sun during the 1919 total solar eclipse provided measurements that confirmed Einstein's general theory of relativity. We have used the Hubble Space Telescope to measure the analogous process of astrometric microlensing caused by a nearby star, the white dwarf Stein 2051 B. As Stein 2051 B passed closely in front of a background star, the background star's position was deflected. Measurement of this deflection at multiple epochs allowed us to determine the mass of Stein 2051 B—the sixth-nearest white dwarf to the Sun—as 0.675 ± 0.051 solar masses. This mass determination provides confirmation of the physics of degenerate matter and lends support to white dwarf evolutionary theory.

One of the key predictions of general relativity set forth by Einstein (*1*) was that the curvature of space near a massive body causes a ray of light passing near it to be deflected by twice the amount expected from classical Newtonian gravity. The subsequent experimental verification of this effect during the 1919 total solar eclipse (*2*, *3*) confirmed Einstein's theory, which was declared "one of the greatest—perhaps the greatest—of achievements in the history of human thought" (*4*).

In a paper in this journal 80 years ago, Einstein (*5*) extended the concept to show that the curvature of space near massive objects allows them to act like lenses, with the possibility of substantially increasing the apparent brightness of a background star. Despite Einstein's pessimistic view that "there is no hope of observing this phenomenon directly" (*5*), the prospect of detecting dark matter through this effect (*6*), now known as microlensing, revived interest in this subject. Coupled with improvements in instrumentation, this led to the detection of large numbers of microlensing brightening events in the Galactic bulge (*7*), the Magellanic Clouds (*8*, *9*), and the Andromeda Galaxy (*10*). Monitoring of these events has led to the discovery of several extrasolar planets (*11*, *12*). Other forms of gravitational lensing by intervening massive galaxies and dark matter produce multiple or distorted images of background galaxies (*13*).

Within the Milky Way, all microlensing encounters discovered so far have been brightening events. No shift in the apparent position of a background star caused by an intervening massive body has been observed outside the solar system—which is not surprising, because the deflections are tiny. Even for the nearest stars, the angular offset is two to three orders of magnitude smaller than the deflection of 1.75 arcsec measured during the 1919 solar eclipse.

Relativistic deflections by foreground stars

When a foreground star (the lens) is perfectly superposed on a background star (the source),

[1]Space Telescope Science Institute, 3700 San Martin Drive, Baltimore, MD 21218, USA. [2]Department of Astronomy and Astrophysics, Pennsylvania State University, University Park, PA 16802, USA. [3]Département de Physique, Université de Montréal, C.P. 6128, Succ. Centre-Ville, Montréal, QC H3C 3J7, Canada. [4]University of St Andrews, School of Physics and Astronomy, North Haugh, St Andrews, KY16 9SS, UK. [5]Department of Physics and Astronomy, University of Nevada, Las Vegas, 4505 South Maryland Parkway, Las Vegas, NV 89154, USA.
*Corresponding author. Email: ksahu@stsci.edu

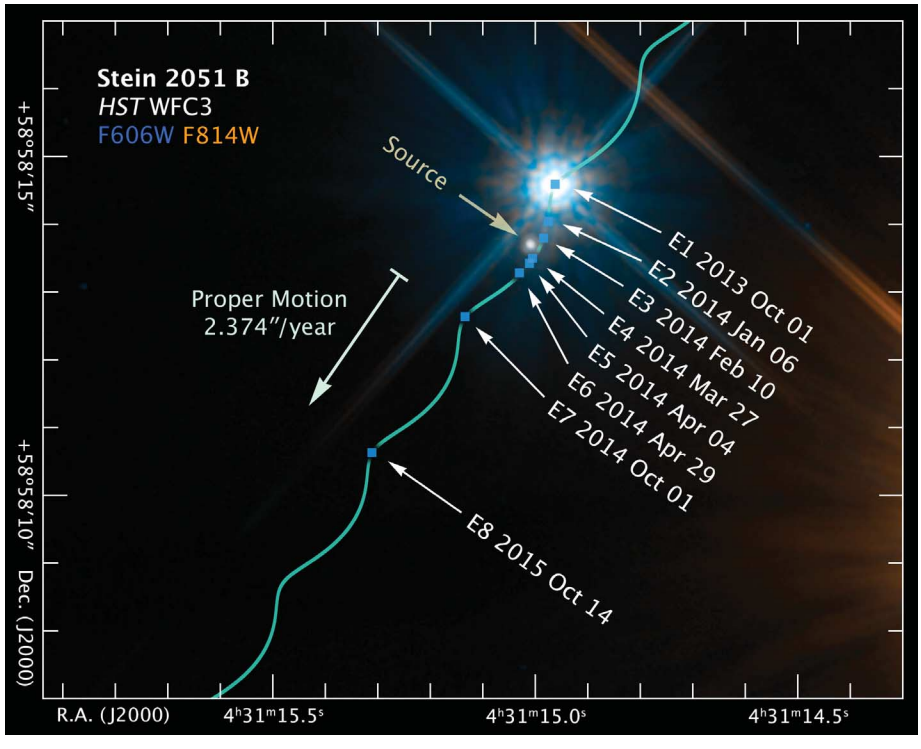

Fig. 1. Hubble Space Telescope image showing the close passage of the nearby white dwarf Stein 2051 B in front of a distant source star. This color image was made by combining the F814W (orange) and F606W (blue) frames, obtained at epoch E1. The path of Stein 2051 B across the field due to its proper motion toward southeast, combined with its parallax due to the motion of Earth around the Sun, is shown by the wavy cyan line. The small blue squares mark the position of Stein 2051 B at each of our eight observing epochs, E1 through E8. Its proper motion in 1 year is shown by an arrow. Labels give the observation date at each epoch. The source is also labeled; the motion of the source is too small to be visible on this scale. Linear features are diffraction spikes from Stein 2051 B and the red dwarf star Stein 2051 A, which falls outside the lower right of the image. Stein 2051 B passed 0.103 arcsec from the source star on 5 March 2014. Individual images taken at all the eight epochs, and an animated video showing the images at all epochs are shown in fig. S1 and movie S1 (*24*).

the lensed image of the source will form a circle, called the Einstein ring. The angular radius of the Einstein ring is (*14*)

$$\theta_E = \sqrt{4GM/c^2 D_r} \quad (1)$$

where M is the lens mass and D_r is the reduced distance to the lens, given by $1/D_r = 1/D_l - 1/D_s$, D_l and D_s being the distances to the lens and to the source, respectively. For typical cases like the Galactic bulge and Magellanic Clouds brightening events, the radius of the Einstein ring is less than a milliarcsecond (mas). However, for very nearby stellar lenses, it can be as large as tens of mas.

In the more general case where the lens is not exactly aligned with the source, the source is split into two images, the minor image lying inside and the major image outside the Einstein ring. The major image is always the brighter, with the brightness contrast increasing rapidly as the lens-source separation increases. In practical cases of lensing by stars, the two images either cannot be resolved or the minor image is too faint to be detected. In both cases, the net effect is an apparent shift in the centroid position of the source. This phenomenon is referred to as astrometric microlensing (*15*).

In cases where the angular separation between the lens and the source is large compared to θ_E, so that the minor image is well resolved but is too faint and too close to the bright lens to be detected, only the major image can be monitored. In that situation, the change in angular position of the source caused by the deflection of the light rays, $\delta\theta$, can be expressed as (*16*)

$$\delta\theta = 0.5\left[\sqrt{(u^2+4)} - u\right]\theta_E \quad (2)$$

where $u = \Delta\theta/\theta_E$, and $\Delta\theta$ is the lens-source angular separation. Equations 1 and 2 show that the mass of the lens can be determined by measuring the deflection of the background source's position at a known angular separation from the lens, provided the reduced distance to the lens is known. Astrometric microlensing thus provides a technique for direct determination of stellar masses, in those favorable cases of a nearby star fortuitously passing closely in front of a distant background source. Unlike classical methods involving binaries, this method can be applied to mass measurements for single stars.

Predicting astrometric microlensing events due to nearby stars

We carried out a large-scale search for events in which nearby stars with large proper motions (PMs) would pass closely in front of background sources. We used an input PM catalog (*17*) of ~5000 stars, with updated positions and PMs based on modern sky-survey data (*18*, *19*). Parallaxes were also included when available. We then projected the positions of all ~5000 stars forward and searched for close passages near fainter background stars contained in the Guide Star Catalog version 2.3 (*20*). One of the predicted events was a close passage of the nearby white dwarf (WD) star Stein 2051 B in front of a background star with V-band magnitude of 18.3, located at right ascension (RA) = 4:31:15.004 and declination (Dec) = +58:58:13.70 (J2000 equinox). This encounter was also predicted in an independent list of upcoming microlensing events (*21*). We estimated that the closest encounter would occur during March 2014, with an impact parameter of ~0″.1.

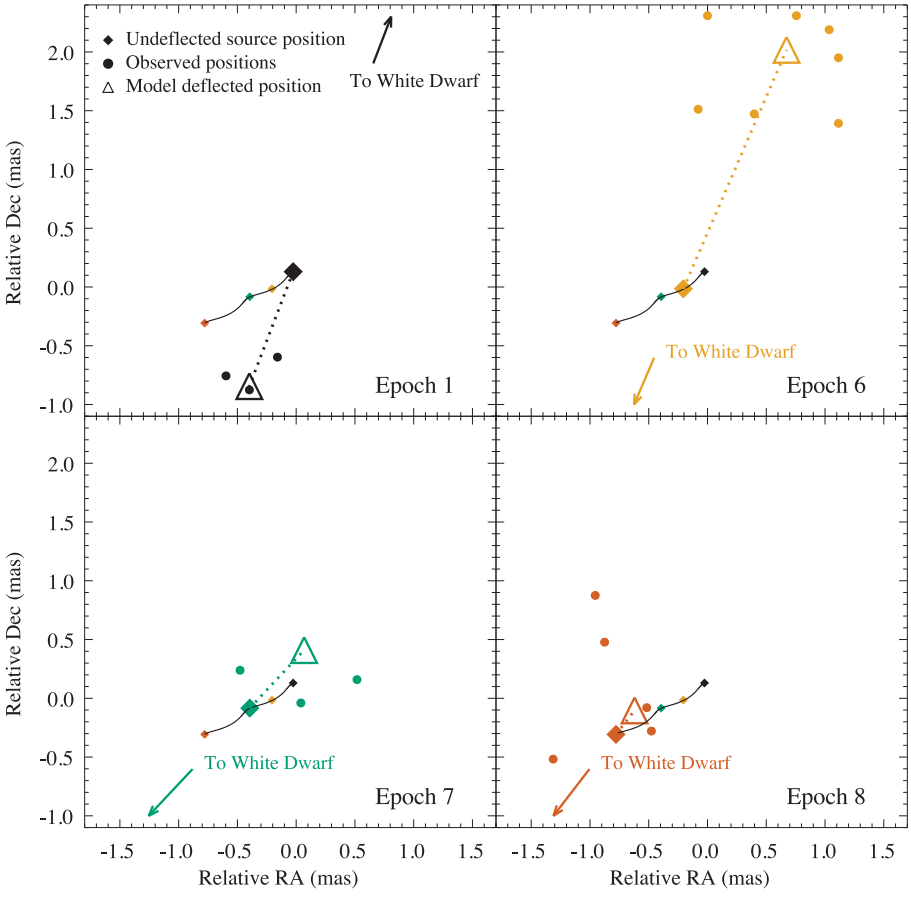

Fig. 2. Hubble Space Telescope measurements of the background star's positions at epochs 1, 6, 7, and 8. The solid dots are the observed positions of the source for each exposure, color-coded for each epoch. The origin corresponds to the undeflected source position at E1, and the relative RA on the *x* axis corresponds to −ΔRA × cos (Dec). The undeflected positions of the source are plotted as solid diamonds, connected with a solid line showing its small parallax and slow proper motion to the southeast. Solid arrows indicate the direction toward the white dwarf at each epoch. At each epoch, the source position is seen to be deflected from its undeflected location, along the direction away from the white dwarf. We modeled the measurements with an Einstein ring of radius 31.53 mas. The model-predicted deflected positions are shown as open triangles, which are joined to the undeflected source positions by dotted lines.

The Stein 2051 binary system

Stein 2051 is a nearby visual binary whose brighter but less-massive component, Stein 2051 A, is an 11th-magnitude (V band) main-sequence star of spectral type M4 (*19*). The 12.4-magnitude companion, Stein 2051 B (also known as WD 0426+588), is the sixth-nearest known WD (*22*). It is currently at an angular separation of ~10″.1 from Stein 2051 A.

Stein 2051 B is the nearest and brightest known featureless-spectrum WD of spectral type DC, having a helium-rich photosphere. We determined its effective temperature to be T_{eff} = 7122 ± 181 K, based on calibrated broadband photometry and model atmospheres (*23*, *24*). Combining the photometry and temperature with the measured parallax (discussed below), we find the radius of the WD to be 0.0114 ± 0.0004 solar radii ($R_\odot$). At this radius, Stein 2051 B would be expected to have a mass of ~0.67 solar masses ($M_\odot$) if it obeys a normal mass-radius relation for carbon-oxygen (CO) core WDs (*25*).

For these parameters, the WD's Einstein ring would have a radius of about 31 mas. At a separation of 0″.5 from Stein 2051 B, the background star would be displaced by ~2 mas. Actual measurement of such a deflection, especially so close to the glare of the bright foreground star, would be extremely challenging for seeing-limited ground-based telescopes. However, the measurement is within the capabilities of the instruments on the Hubble Space Telescope (HST).

Table 1. Details of the HST Observations. The numbers in the "No. of exp." column correspond to the number of exposures taken with the corresponding "Exp. time" specified in the previous column. The last column gives the projected separation between the lens and the undeflected position of the source.

Epoch	Obs. date	Filter	Subarray size (pixels)	Exp. time (s)	No. of exp.	Lens-source separation (")
1	1 Oct 2013	F814W	2048 × 2048	0.5/250	2/3	0.943
		F606W	2048 × 2048	0.5/250	2/2	
2	6 Jan 2014	F814W	2048 × 2048	1/270	2/3	0.434
		F606W	2048 × 2048	0.5/270	2/2	
3	10 Feb 2014	F814W	1024 × 1024	1/50	3/3	0.203
		"	2048 × 2048	1/50	1/1	
		F763M	512 × 512	2/90	11/11	
4	27 Mar 2014	F814W	1024 × 1024	1/50	3/3	0.205
		"	2048 × 2048	1/50	1/1	
		F763M	512 × 512	0.5/8	11/19	
5	4 Apr 2014	F814W	1024 × 1024	1/50	3/3	0.262
		"	2048 × 2048	1/50	1/1	
		F763M	512 × 512	0.5/8	11/19	
6	29 Apr 2014	F814W	1024 × 1024	2/3/75	8/8/8	0.462
7	1 Oct 2014	F814W	2048 × 2048	1/240	3/3	1.478
		F606W	2048 × 2048	0.5/240	2/2	
8	14 Oct 2015	F814W	2048 × 2048	1/240	3/5	3.897
		F763M	2048 × 2048	0.5	2	

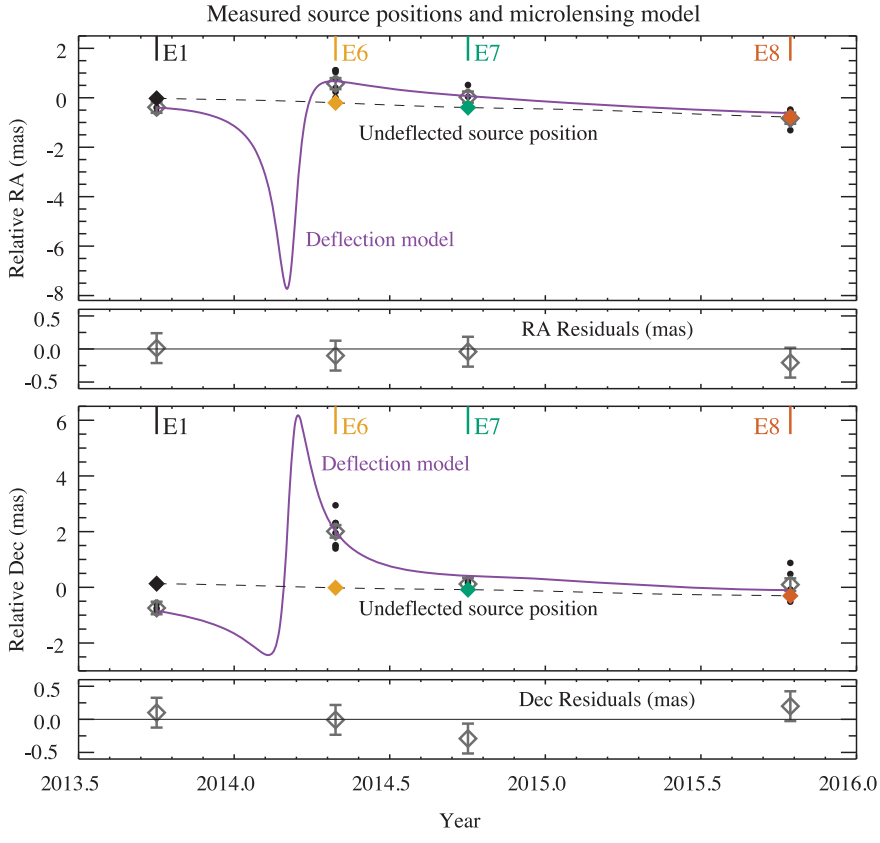

Fig. 3. Measured and model undeflected RA and Dec positions of the background source as a function of time. The positions are relative to the undeflected source position at E1. Solid diamonds show the undeflected positions, color-coded with the same colors as in Fig. 2 and connected by dashed lines showing the small parallax and proper motion. The measured deflected positions are plotted as filled black circles, and their mean at each epoch is shown as a diamond along with the standard deviations of the mean. Our model fit, with an Einstein ring radius of 31.53 mas, is shown as a solid purple curve. The RA and Dec residuals after subtracting the model from the mean observed positions are shown in separate panels.

The actual mass of Stein 2051 B has been a matter of debate. Photographic observations extending back to 1908 have been used to claim departures from linear PMs of A and B (*26*, *27*), implying a detection of orbital motion and a mass ratio of M_B/M_A = 2.07. Assuming A to be a normal M4 main-sequence star of 0.24 $M_\odot$, the mass of B was estimated (*26*, *27*) to be 0.50 $M_\odot$. A mass this low, combined with its inferred radius, would lead to the requirement for the WD to have an iron core. Such a result would be in conflict with normal single-star evolution, in which the stellar core only undergoes hydrogen and then helium fusion, resulting in a CO core composition for the WD remnant (*25*). Moreover, a WD cooling age of ~2.0 billion years (Gy) derived for Stein 2051 B (*22*), combined with the implied long main-sequence lifetime of the progenitor of a low-mass WD (*28*), would give the system a total age uncomfortably close to the age of the universe. However, the detection of nonlinear PMs was not confirmed by subsequent measurements (*29*), implying that the orbital period of the A-B pair exceeds ~1000 years, and appearing to invalidate the earlier mass determination.

Hubble Space Telescope observations and analysis

We imaged the field of Stein 2051 with the Wide Field Camera 3 at eight epochs (denoted E1 through E8) between October 2013 and October 2015. The HST observing log is given in Table 1. We employed a range of exposure times (*24*), depending on how close the WD was to the source star, in three filters: F606W (a wide V band), F763M (a medium red band), and F814W (equivalent to I band). We used the long-exposure broadband F606W and F814W images for the deflection measurements of the source star. For determining the location of the WD, we used short-exposure F606W and

F814W images and all the F763M frames (in which the WD did not saturate the detector).

Figure 1 shows a color image of the region around Stein 2051 B, created by superposing F606W and F814W frames at epoch E1. The path of the WD past the source, due to PM and parallax, is depicted by the wavy line. Closest approach to the source star occurred on 5 March 2014, at an angular separation of 103 mas. Even at closest separation, the photometric microlensing amplification would be only 1.0% and thus swamped by light from the bright WD, so we did not attempt to measure it. For measurements of the deflection, we obtained data at separations ranging from 203 to 3897 mas. (The amplification at our observed minimum separation of 203 mas is even less, 0.1%, which is undetectable.) We used the observations at all eight epochs to determine the parallax and PM of the WD. However, the presence of the 400-times-brighter WD adjacent to the faint source made the deflection measurements possible only at separations larger than ~450 mas. In the epoch E2 frames, the source lay on a diffraction spike of the WD, and consequently the measurements had large uncertainties of ~0.1 pixels. We thus used only the observations taken at epochs E1, E6, E7, and E8 for the deflection analysis.

Full details of our data-analysis procedures are given in the online supplementary material (*24*), but we summarize them here. We used the flat-fielded images produced by the Space Telescope Science Institute pipeline reductions (*30*) for the analysis. We used empirical effective point spread functions (PSFs) (*31*) to measure the positions of the 26 reference stars in the surrounding field, and then applied distortion corrections (*32*) to convert the measured positions into locations in an undistorted reference frame. We used empirical PSFs to determine the source positions at epochs E1, E7, and E8, during which the source was sufficiently separated from the WD that it did not suffer from any contamination from the WD. At E6, when the source was 11.3 pixels away from the WD, the contamination from the WD was estimated to be about 5% of the source flux. We therefore performed an optimal PSF subtraction of the WD before measuring the position of the source (*24*).

We estimated distances to the reference stars and source by obtaining their magnitudes and colors determined from our HST frames, the Panoramic Survey Telescope and Rapid Response System (Pan-STARRS) survey (*33*), and the Two Micron All Sky Survey (2MASS) (*34*). Theoretical stellar models (*35*) were then used to determine individual distances of the reference stars, which lie in the range ~0.8 to 2.1 kiloparsecs (kpc). The source itself is estimated to be a K dwarf at a distance of ~2.0 kpc.

To establish a fixed reference frame, we first determined the PM of each reference star with respect to the ensemble, using an iterative procedure (*24*). Then at each epoch, the reference-star positions were corrected for PM, and the positions of the source and the WD were determined relative to this adjusted frame. The estimated uncertainty in the position of the source star relative to the adjusted frame is ~0.4 mas in each individual exposure.

Parallax and proper motion of Stein 2051 B

From our measurements of Stein 2051 B at the eight epochs, we find a parallax of 180.7 ± 1.0 mas relative to the background frame, or an absolute parallax of 181.5 ± 1.0 mas after correction by the mean of our estimated reference-star parallaxes of 0.8 ± 0.2 mas. Absolute parallaxes for the Stein 2051 system have been measured previously (*36*–*38*), giving a weighted mean of 180.9 ± 0.5 mas, in statistical agreement with our result. The corresponding distance is 5.52 ± 0.01 parsecs (pc). We measure PM components for Stein 2051 B of $(\mu_\alpha, \mu_\delta) = (+1336.3 \pm 1.0, -1947.5 \pm 1.0)$ mas year^{-1}, where μ_α is the PM in the RA direction and μ_δ is the PM in the Dec direction. These again are not absolute, but relative to our background reference frame. The PM of Stein 2051 B relative to a different selection of nearby reference stars has been measured previously to be $(\mu_\alpha, \mu_\delta) = (+1361.8 \pm 2.0, -1930.4 \pm 2.0)$ mas year^{-1} (*36*), and the absolute PM to be $(\mu_\alpha, \mu_\delta) = (+1335.6 \pm 2.5, -1962.6 \pm 2.5)$ mas year^{-1} (*39*). The differences between these values show sensitivity to the bulk motion of the chosen reference frame, but do not affect our interpretation of the event as long as our measurements are consistently in the same reference frame for both the source and the WD (*24*). The position of the WD at each epoch relative to our reference frame is thus known to an accuracy that will cause only a small additional uncertainty of $\lesssim$0.5% of its mass derived from the relativistic deflection of the source, even at the E6 separation of 0″.46 (*24*). Combined with its radial velocity of +29 km s^{-1} (*40*), the total space velocity of the Stein 2051 system is 68.8 km s^{-1} with respect to the Sun.

Relativistic deflection and mass of Stein 2051 B

Figure 2 plots the measured source positions at the four epochs that we analyzed, showing the relativistic deflections. At each epoch, they are in the direction away from the foreground WD, and by an amount inversely proportional to the angular distance between the source and the WD, as expected from Eq. 2.

We performed a model fit to the observed shifts shown in Fig. 2 using six parameters: the initial RA and Dec positions of the source, its two PM components along RA and Dec, its parallax with respect to the reference frame used, and θ_E, and adopting a chi-square minimization approach (*41*). An additional constraint is that the deflection must lie along the line joining the WD and the source. Fitting this model to the 19 pairs of observed RA/Dec positions at the four useful epochs yields the predicted positions shown in Fig. 2. The observed positions are consistent with the positions expected from the model within the measurement uncertainties. The time evolution of the angular shifts is also consistent with our model (Fig. 3).

The resulting fitting parameters of our model are a source PM of $(\mu_\alpha, \mu_\delta) = (-0.4 \pm 0.05, +0.2 \pm 0.05)$ mas year^{-1}, a parallax of 0.25 ± 0.1 mas with respect to the mean parallax of the reference stars, and an Einstein ring radius of $\theta_E = 31.53 \pm 1.20$ mas. Using Eq. 1 and the measured parallax, we find Stein 2051 B to have a mass of 0.675 ± 0.051 $M_\odot$.

Astrophysics of the cool white dwarf Stein 2051 B

Most stars end their lives as WDs—as will the Sun—and then slowly cool. Composed of degenerate

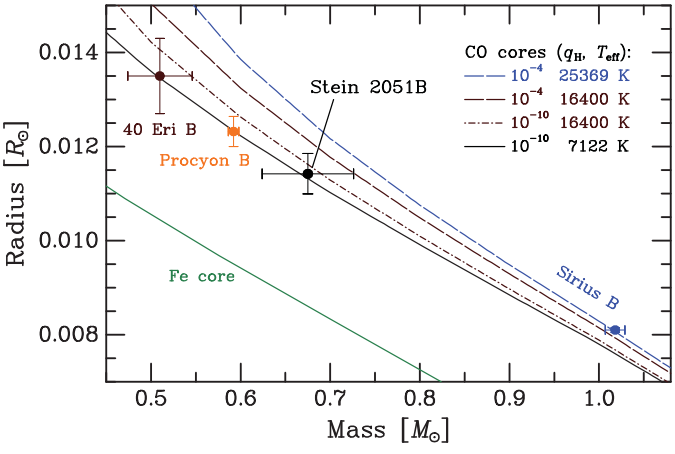

Fig. 4. Mass-radius diagram for Stein 2051 B and three nearby white dwarfs in visual binaries. Data points with error bars show the masses and radii for Stein 2051 B (this paper; black), 40 Eridani B [(*43*); dark brown], Sirius B [(*46*); blue)], and Procyon B [(*47*); orange]. The black curve plots a theoretical mass-radius relation (*23*) for carbon-oxygen core white dwarfs with the parameters of Stein 2051 B (thin hydrogen layer, $q_H = M_H/M_{WD} = 10^{-10}$; effective temperature 7122 K). This curve is also appropriate for the similar white dwarf Procyon B. The blue curve shows the relation (*23*) for thick hydrogen-layer CO white dwarfs with the effective temperature of Sirius B, and the dark brown curves plot the relations for thick and thin hydrogen-layer CO white dwarfs with the temperature of 40 Eri B. The green curve shows the theoretical relation for zero-temperature white dwarfs with iron cores (*48*). The mass of Stein 2051 B inferred from the astrometric microlensing, 0.675 ± 0.051 $M_\odot$, is consistent with the CO core expected from normal stellar evolution.

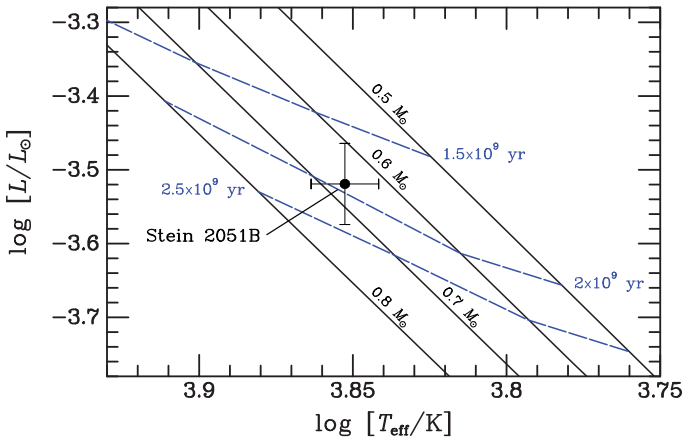

Fig. 5. Theoretical WD cooling tracks (*23*). Cooling tracks are shown for four masses (solid lines), along with isochrones showing the WD cooling ages (dashed lines). The position of Stein 2051 B agrees within the uncertainties with that expected for our measured mass. The implied cooling age of Stein 2051 B is 1.9 ± 0.4 Gy.

matter, WDs are expected to obey a mass-radius relation (MRR) such that, as the mass of the WD increases from ~0.5 $M_\odot$ to the Chandrasekhar limit of ~1.4 $M_\odot$ (*42*), its radius decreases approximately as the inverse cube root of its mass (*43*). The MRR has a relatively large dependence on core composition, and smaller dependencies on photospheric composition, thicknesses of the H and/or He envelopes lying above the degenerate interior, and a continued small amount of shrinkage as the WD gradually cools (*44*). The vast majority of WD masses cannot be measured directly, but have to be inferred from model-dependent determinations of their surface gravities and estimates of their radii from parallax determinations and photometric or spectroscopic flux measurements (*44*), or from gravitational redshifts in cases where the true radial velocity of the WD is known from measurements of a companion star (*45*). The number of WDs whose masses and radii have been directly measured with sufficient precision to test theoretical MRRs includes just three WDs in nearby wide visual binaries [Sirius B (*46*), Procyon B (*47*), and 40 Eri B (*43*)] and about 10 WDs in short-period eclipsing binaries (*44*). However, the stars in the latter group have undergone common-envelope events and have therefore not evolved in the same way as isolated single stars. The mass of a WD in a transiting binary system with an 88-day orbital period was recently measured through the photometric microlensing caused by the WD as it periodically passes in front of the G-dwarf companion (*48*).

Our direct measurement of the mass of Stein 2051 B, with an uncertainty of 0.051 $M_\odot$, provides an additional data point for comparison with theoretical MRRs and evolutionary cooling tracks. The location of Stein 2051 B in the MRR is shown in Fig. 4. We overlay an MRR for He-atmosphere, CO-core WDs (*23*) interpolated to the effective temperature of Stein 2051 B. For comparison, the MRR for zero-temperature WDs with iron cores (*49*) is also shown, but is excluded by our measurement. For a CO core, the diagram shows that our radius determination implies an expected mass of Stein 2051 B of 0.67 ± 0.03 $M_\odot$, in agreement with our measured value of 0.675 ± 0.051 $M_\odot$.

The position of Stein 2051 B in the theoretical Hertzsprung-Russell diagram (luminosity versus surface effective temperature) is shown in Fig. 5, along with evolutionary cooling sequences with their cooling ages marked for CO-core WDs of masses 0.5 to 0.8 $M_\odot$ (*23*). These models have thin H ($M_H/M_{WD} = 10^{-10}$) layers, which are appropriate for helium-atmosphere compositions. The implied WD cooling age of Stein 2051 B is 1.9 ± 0.4 Gy. The progenitor of the WD had a mass of 2.6 ± 0.6 $M_\odot$, based on a recent determination of the initial-mass/final-mass relation (*50*). The corresponding theoretical pre-WD evolutionary lifetimes of these progenitors range from 0.4 to 1.3 Gy (*51*). Combining these with the cooling age, we find that the Stein 2051 system has a total age in the range of 1.9 to 3.6 Gy. Unlike previous conclusions of an iron core WD, our measurement does not conflict with the age of the universe. The derived age of the system is consistent with its moderately high space velocity, suggesting that it may be a member of the Galaxy's thick disk.

REFERENCES AND NOTES

1. A. Einstein, *Ann. Phys.* **354**, 769–822 (1916).
2. F. W. Dyson, A. S. Eddington, C. Davidson, *Philos. Trans. R. Soc. London A* **220**, 291–333 (1920).
3. C. M. Will, *Living Rev. Relativ.* **17**, 4 (2014).
4. *New York Times*, "Eclipse showed gravity variation: Diversion of light rays accepted as affecting Newton's principles, hailed as epochmaking," 8 November 1919, p. 6.
5. A. Einstein, *Science* **84**, 506–507 (1936).
6. B. Paczyński, *Astrophys. J.* **304**, 1–5 (1986).
7. A. Udalski *et al.*, *Acta Astron.* **43**, 289–294 (1993).
8. C. Alcock *et al.*, *Nature* **365**, 621–623 (1993).
9. E. Aubourg *et al.*, *Nature* **365**, 623–625 (1993).
10. S. Calchi Novati *et al.*, *Astron. Astrophys.* **381**, 848–861 (2002).
11. J.-P. Beaulieu *et al.*, *Nature* **439**, 437–440 (2006).
12. B. S. Gaudi, *Annu. Rev. Astron. Astrophys.* **50**, 411–453 (2012).
13. T. Treu, *Annu. Rev. Astron. Astrophys.* **48**, 87–125 (2010).
14. B. Paczyński, *Annu. Rev. Astron. Astrophys.* **34**, 419–459 (1996).
15. M. Dominik, K. C. Sahu, *Astrophys. J.* **534**, 213–226 (2000).
16. K. C. Sahu, H. E. Bond, J. Anderson, M. Dominik, *Astrophys. J.* **782**, 89 (2014).
17. W. J. Luyten, *LHS Catalog*, Univ. of Minnesota, Minneapolis (1979).
18. G. Bakos, K. C. Sahu, P. Nemeth, *Astrophys. J. Suppl. Ser.* **141**, 187–193 (2002).
19. S. Lépine, M. M. Shara, *Astrophys. J.* **129**, 1483–1522 (2005).
20. B. M. Lasker *et al.*, *Astron. J.* **136**, 735–766 (2008).
21. S. Proft, M. Demleitner, J. Wambsganss, *Astron. Astrophys.* **536**, A50 (2011).
22. N. Giammichele, P. Bergeron, P. Dufour, *Astrophys. J. Suppl. Ser.* **199**, 29 (2012).
23. P. Bergeron *et al.*, *Astrophys. J.* **737**, 28 (2011).
24. Materials and methods are available as supplementary materials.
25. J. L. Provencal, H. L. Shipman, E. Høg, P. Thejll, *Astrophys. J.* **494**, 759–767 (1998).
26. K. A. Strand, *Astron. J.* **82**, 745–749 (1977).
27. K. Strand, V. Kallarakal, in *White Dwarfs*, Proceedings of IAU Colloquium 114 (Springer, 1989), pp. 413–415.
28. J. Kalirai *et al.*, *Astrophys. J.* **676**, 594–609 (2008).
29. W. D. Heintz, *Astron. J.* **99**, 420–423 (1990).
30. L. Dressel, *Wide Field Camera 3 Instrument Handbook*, version 6.0 (Space Telescope Science Institute, Baltimore, 2014.).
31. J. Anderson, I. King, *Publ. Astron. Soc. Pac.* **115**, 113–131 (2003).
32. A. Bellini, J. Anderson, L. R. Bedin, *Publ. Astron. Soc. Pac.* **123**, 622–637 (2011).
33. K. C. Chambers *et al.*, The Pan-STARRS1 Surveys. arXiv:1612.05560 [astro-ph.IM] (2016).
34. M. F. Skrutskie *et al.*, *Astron. J.* **131**, 1163–1183 (2006).
35. L. Girardi, A. Bressan, G. Bertelli, C. Chiosi, *Astron. Astrophys. Suppl. Ser.* **141**, 371–383 (2000).
36. R. S. Harrington *et al.*, *Astron. J.* **105**, 1571–1580 (1993).
37. F. van Leeuwen, *Astron. Astrophys.* **474**, 653–664 (2007).
38. A. G. A. Brown *et al.*, *Astron. Astrophys.* **595**, A2 (2016).
39. N. Zacharias *et al.*, *Astron. J.* **145**, 44 (2013).
40. E. R. Newton *et al.*, *Astron. J.* **147**, 20 (2014).
41. P. R. Bevington, D. K. Robinson, *Data Reduction and Error Analysis* (McGraw Hill, New York, ed. 3, 2003), chap. 8.
42. S. Chandrasekhar, *Mon. Not. R. Astron. Soc.* **95**, 207–225 (1935).
43. J. B. Holberg, T. D. Oswalt, M. A. Barstow, *Astron. J.* **143**, 68 (2012).
44. P.-E. Tremblay *et al.*, *Mon. Not. R. Astron. Soc.* **465**, 2849–2861 (2017).
45. M. A. Barstow *et al.*, *Mon. Not. R. Astron. Soc.* **362**, 1134–1142 (2005).
46. H. E. Bond *et al.*, *Astrophys. J.* **840**, 70 (2017).
47. H. E. Bond *et al.*, *Astrophys. J.* **813**, 106 (2015).
48. E. Kruse, E. Agol, *Science* **344**, 275–277 (2014).
49. T. Hamada, E. E. Salpeter, *Astrophys. J.* **134**, 683–698 (1961).
50. J. D. Cummings, J. S. Kalirai, P.-E. Tremblay, E. Ramirez-Ruiz, *Astrophys. J.* **807**, 90 (2015).
51. J. Choi *et al.*, *Astrophys. J.* **823**, 102 (2016).

ACKNOWLEDGMENTS

Based in part on observations made with the NASA–European Space Agency Hubble Space Telescope, obtained at Space Telescope Science Institute (STScI), which is operated by the Association of Universities for Research in Astronomy under NASA contract NAS 5-26555. HST data used in this paper are available from the Mikulski Archive for Space Telescopes at STScI (https://archive.stsci.edu/hst/search.php), under proposal ID 13457 and 14448. Support for this program was provided by NASA through a grant from STScI. We thank J. Mack and M. Sosey for help with image processing, P.-E. Tremblay for useful discussions, A. Rest for assistance with the Pan-STARRS data, D. Taylor for support with the observations, and G. Bacon for help with the preparation of an animated movie. The Pan-STARRS1 Surveys (PS1) have been made possible through contributions of the Institute for Astronomy, the University of Hawaii, the Pan-STARRS Project Office, the Max Planck Society and its participating institutes, Johns Hopkins University, Durham University, the University of Edinburgh, Queen's University Belfast, the Harvard-Smithsonian Center for Astrophysics, the Las Cumbres Observatory Global Telescope Network Incorporated, the National Central University of Taiwan, the Space Telescope Science Institute, NASA Administration under grant no. NNX08AR22G, the National Science Foundation under grant no. AST-1238877, the University of Maryland, and Eotvos Lorand University. M.D. thanks Qatar National Research Fund (QNRF) for support by grant NPRP 09-476-1-078.

SUPPLEMENTARY MATERIALS

www.sciencemag.org/content/356/6342/1046/suppl/DC1
Materials and Methods
Supplementary Text
Table S1
Figs. S1 to S10
References (*52*–*57*)
Movies S1 and S2

26 October 2016; accepted 24 April 2017
Published online 7 June 2017
10.1126/science.aal2879

Relativistic deflection of background starlight measures the mass of a nearby white dwarf star

Kailash C. Sahu, Jay Anderson, Stefano Casertano, Howard E. Bond, Pierre Bergeron, Edmund P. Nelan, Laurent Pueyo, Thomas M. Brown, Andrea Bellini, Zoltan G. Levay, Joshua Sokol, Martin Dominik, Annalisa Calamida, Noé Kains and Mario Livio

Science **356** (6342), 1046-1050.
DOI: 10.1126/science.aal2879originally published online June 7, 2017

General relativity weighs a white dwarf

Light from a background star is deflected by the gravitational field of the Sun. This effect was used in 1919 to provide some of the first evidence for general relativity. Sahu *et al.* applied the concept to another star: a nearby white dwarf called Stein 2051 B, which passed close in front of a more distant normal star (see the Perspective by Oswalt). The authors measured the tiny shifts in the apparent position of the background star, an effect called astrometric microlensing. The apparent motion matched the predictions of general relativity, which allowed the authors to determine the mass of the white dwarf.

Science, this issue p. 1046; see also p. 1015